Studying Catalytically Viable Single Crystalline Metal Oxide Nanorods Using Synchrotron-Based Scanning Hard X-ray Microscopy

Luyao Li,[1] Sha Tan,[1] Shiyu Yue,[1] Hanfei Yan,[2] Yong S. Chu,[2] Xiao Tong,[3] and Stanislaus S. Wong[1,*]

Email: stanislaus.wong@stonybrook.edu; sswong@bnl.gov

[1]Department of Chemistry, State University of New York at Stony Brook, Stony Brook, NY 11794-3400

[2]National Synchrotron Light Source II, Building 743, Brookhaven National Laboratory, Upton, NY 11973

[3]Center for Functional Nanomaterials, Building 735, Brookhaven National Laboratory, Upton, NY 11973

*To whom correspondence should be addressed.

Abstract: Synchrotron-based scanning hard X-ray microscopy (SHXM) was used to extract localized chemical and structural information within a system of model alkaline-earth-metal tungstate nanorods, characterized by multiple chemical configurations. Specifically, we have highlighted the practical ability of SHXM to probe chemically distinctive nanoscale species, i.e. (i) chemically-doped versus (ii) solid-solution-state nanorods of comparable dimension, synthesized using a template-directed method under ambient conditions. Indeed, we show that SHXM can be used to map out elemental distributions within individual anisotropic nanorods with nanoscale resolution, coupled with chemical sensitivity and specificity. Complementary electrochemical results suggest the possibility of using these nanorods as support materials for electro-oxidation reactions within an acidic electrolyte medium. Our structural and chemical composition results have been corroborated using parallel lines of inquiry involving scanning electron microscopy, transmission electron microscopy, energy dispersive X-ray spectroscopy, X-ray diffraction, and X-ray photoelectron spectroscopy. These measurements confirmed the relatively even and uniform distribution of the expected, individual elements within all of the nanorod samples tested.

1. Introduction

Intrinsic sample properties, including chemical composition, lattice dimensions, crystallographic symmetry, size, shape, and morphology often dictate observed behavior, whether it be electronic, magnetic, optical, or catalytic, of relevance for applications.[1] As an illustrative example, in a recent Perspective article,[2] we and others have noted that to achieve dramatic progress in understanding and improving upon practical fuel cells required the ability to probe and to understand the nuances associated with precisely, synergistically, and simultaneously tuning the chemical composition and physical structure of the individual components of the entire 'catalyst-support' system. Therefore, advancing our understanding of materials and their role within functional material systems necessitates a fundamental assessment of the strengths and limitations of various characterization techniques, especially relatively new but interesting ones. Indeed, devising useful structure-property correlations relies upon gaining a broader perspective by taking a 'step back' in the sense of acquiring and interpreting complementary and usable data streams about the distinctive chemical and physical attributes of target materials.

Conventional microscopy methods such as transmission electron microscopy (TEM) and scanning electron microscopy (SEM) have been reliably utilized to generate data about sample morphology, structure, dimensionality, and uniformity. X-ray diffraction (XRD) and selected area electron diffraction (SAED) yield complementary insights into chemical composition, unit cell content, lattice orientation, and degree of crystallinity. Additional techniques such as X-ray photoelectron spectroscopy (XPS) and energy dispersive X-ray spectroscopy (EDS) can also collectively provide important information about chemical composition and electronic structure.

While each of these prior methods is well understood, highly ubiquitous, and clearly useful, it is understandably more difficult to achieve interpretable data on chemical composition and physical morphology, not only simultaneously but also with relevant spatial resolution. To try to address these issues, in this paper, we have applied a synchrotron-based scanning hard X-ray microscopy (SHXM) with reasonable spatial resolution, using the Nanoscale Multimodal Imaging (Nano-Mii) Instrument situated at the Hard X-ray Nanoprobe (HXN) Beamline[3-4] at the National Synchrotron Light Source II (NSLS-II). Specifically, we have acquired not only high-resolution fluorescence images but also complementary differential phase contrast (DPC) data,[5-6] that correlate with chemical and morphological changes within our targeted model systems.

As a specific material worth investigating, alkaline-earth metal tungstates AWO_4 (A = Ca, Sr, Ba)[7-9] possess a distinctive scheelite structure with implications for their traditional incorporation as components of inorganic, electro-optic materials.[8-9] We have discovered a number of interesting phenomena in these systems. That is, we (i) measured compositionally-modulated luminescence properties over several distinctive series (i.e., $Sr_{1-x}Ca_xWO_4$ and $Ba_{1-x}Sr_xWO_4$ ($0 \leq x \leq 1$)) of as-prepared, homogeneous solid-solution nanorods[10] and (ii) found that in uniform Mn-doped AWO_4 (A = Ca, Sr, Ba) nanorods, the presence of Mn^{+2} not only substantially increased its photoluminescent signature but also rendered it as simultaneously magnetic.[11] Indeed, our choice of tungstates is motivated by recent and parallel thematic efforts in our group, seeking to use metal oxides (including ternary perovskites) either as co-catalysts or as underlying supports[12] which can thereby give rise to beneficial metal-support interactions with their overlying metal catalysts[13-14] within electrocatalytically-relevant systems. Significantly, anisotropic tungsten oxide nanorods have been reported as effective catalyst supports[15-17] as a means of enhancing Pt utilization for the methanol oxidation reaction (MOR). Moreover,

tungstates have been considered as unconventional but promising candidates for use in energy storage devices,[18] syngas production through methane oxidation,[19-20] pollutant remediation,[18] green chemical approaches to one-pot organic synthesis reactions,[21] and the oxygen reduction reaction.[22-23] The key lesson learned from that all of these various examples of viable applications of tungstates is that in addition to morphology, slight variations in chemical composition coupled with spatial fluctuations in chemical content throughout that physical structure can be considered as determinants of observed functionality.

As an illustrative 'function' worth exploring, we have been primarily interested in analyzing the electrochemical performance of Ba-based tungstates. In particular, to probe the potential of utilizing tungstates as support materials towards the electro-oxidation of methanol, we have fabricated a series of related samples including (i) Mn-doped $BaWO_4$ (designated herein as 'Mn-$BaWO_4$') nanorods, (ii) $Ba_{0.5}Sr_{0.5}WO_4$ (denoted herein as '$BaSrWO_4$') nanorods, (iii) pure $BaWO_4$ controls, and (iv) pure $SrWO_4$ control samples, using a well-developed, 'hard-template'-based method.[24] SHXM, with its high elemental sensitivity and associated capability of achieving deep penetration within the sample itself, was used to map out the elemental distributions of each of these tungstate samples, and these results provided for a set of useful characterization data on these materials, prior to electrochemical testing.

We have demonstrated for the first time that Ba-based tungstates are indeed electrochemically stable within acidic media, with implications for their use as possible catalyst supports. Moreover, we have shown that the main advantage of using SHXM on our nanoscale systems has been to provide simultaneous insights into morphology, surface structure, and overall elemental distribution.

2. Methods

Synthesis

Chemicals. Precursors were acquired, as follows. Sodium tungstate dihydrate ($Na_2WO_4 \cdot 2H_2O$, Sigma BioUltra, ≥99.0%), barium chloride ($BaCl_2$, J.T. Baker Chemical), strontium chloride hexahydrate ($SrCl_2 \cdot 6H_2O$, Alfa Aesar, 99.0%-103.0%), manganese nitrate tetrahydrate ($MnN_2O_6 \cdot 4H_2O$, Alfa Aesar, 98.0%), octadecyltrichlorosilane (Sigma Aldrich, ≥90%), *n*-hexane (Alfa Aesar, Spectrophotometric grade, 95+%), dichloromethane (Sigma Aldrich, anhydrous ≥99.8%), and reagent alcohol (VWR Chemical, 95%, for washing) were purchased and used, as received, without additional purification protocols.

Synthesis of various AWO_4 (A = Ba, Sr) nanorods. Our model system of alkaline-earth-metal tungstate nanorods was generated in a wet-chemical environment at room temperature under ambient conditions through the mediation of a hard-template-based method, as previously reported by our group.[10-11] In a typical synthesis, track-etched polycarbonate (PC) - based membranes, measuring 6 μm in thickness and maintaining average pore sizes of 200 nm in diameter, were initially immersed and sonicated in de-ionized water for 10 minutes so as to remove air bubbles that may have possibly formed either within the membrane pores or on the external surfaces of the membrane surfaces themselves. The PC templates were subsequently dried in air, prior to reaction. These membranes served as spatially confined reaction vessels for the production of the desired nanorods.

To prevent the unwanted formation of extraneous particles on the external surfaces of the reagent PC membranes, the external surfaces of these polymeric templates were treated with microcontact-printed OTS-SAMs (octadecyltetrachlorosilane self-assembled monolayers). This procedure, which created hydrophobic passivation layers, was indispensable to rendering these

surfaces less susceptible to undesirable side-reactions. As such, a 10 mM *n*-hexane solution of OTS was prepared and then inked with a home-made polydimethylsiloxane (PDMS) stamp. The stamp was subsequently placed into contact with the PC templates for ~30 s, and later peeled off. The surface-modified PC template was carefully mounted between two half-arms within a U-shaped tube cell (Figure S1).

To fabricate pure tungstate samples, one 'half-arm' of a home-made U-tube cell was filled with an aqueous-based Na_2WO_4 solution, whereas the other corresponding 'half-cell' was permeated with an analogous metal ion-based (i.e. either Ba or Sr) solution, in order to fabricate individual $BaWO_4$ and $SrWO_4$ nanorods, respectively. The U-shaped tube cell was left alone in order to react at room-temperature for an incubation time of 24 h. After the reaction process was completed, the PC membrane was removed and mechanically polished to eliminate any undesirable bulk materials that may have collected on the template surfaces. After a thorough washing with DI water to purge the membrane of any inorganic impurities, it was later dissolved in a solution of methylene chloride. As such, the final, desired nanowire product could be ultimately collected by centrifugation, after washing with aliquots of ethanol.

Synthesis of $Ba_{0.5}Sr_{0.5}WO_4$ and Mn-doped $BaWO_4$ nanorods. Nanorod samples, consisting of (i) a more compositionally complex tungstate, composed of a stoichiometrically targeted cationic mixture of barium and strontium, along with (ii) manganese (Mn) - doped tungstate, were prepared under identical conditions, except for the use of different metal ion-containing solutions. Specifically, the solid-solution sample of $Ba_{0.5}Sr_{0.5}WO_4$ was produced by combining $BaCl_2$ and $SrCl_2 \cdot 6H_2O$ precursors in equimolar amounts and adding these to one of the half-cells. By analogy, Mn-doped $BaWO_4$ nanorods were fabricated by blending in an aqueous solution,

comprised of $BaCl_2$ dispersed together with $MnN_2O_6 \cdot 4H_2O$, with the latter set at an overall concentration of 10 mol%, within one of the reagent half-cells.

Structural Characterization Techniques

X-ray diffraction (XRD). XRD samples were prepared by dispersing as-prepared nanorod powders in ethanol and then drop casting aliquots onto a zero-background holder (MTI Corporation, Zero diffraction plate for XRD, B-doped, *p*-type Si, measuring 23.6 mm in diameter by 2 mm in thickness). Diffraction pattern data were obtained on a Scintag diffractometer, operating in the Bragg-Brentano configuration with Cu $K\alpha_1$ irradiation ($\lambda = 1.54$ Å). All of these results were collected from 10° to 90° in the Bragg configuration with scanning rate at 10^o per minute. In effect, XRD was used to verify crystalline phases and the possibility of sample purities. To assist in the identification process, acquired diffraction peaks for each of the various crystalline planes were systematically and individually indexed.

Transmission electron microscopy (TEM). Typical low-resolution TEM images of as-fabricated nanorods were amassed using a JEOL 1400 transmission electron microscope, equipped with a 2048 × 2048 Gatan CCD camera and operating at an accelerating voltage of 120 kV. To assist in sample acquisition, relevant sample powders were dispersed in ethanol and then drop cast onto a commercial carbon-coated Cu grid. Isolated morphologies were directly observable through acquired TEM images. Feature dimensions were measured using the ImageJ software.

High-resolution transmission electron microscopy (HRTEM) and selected area electron diffraction (SAED). HRTEM images and associated SAED patterns were collected on a JEOL 2100F instrument, which had been operating at accelerating voltages of 200 kV with a beam size of 2 Å. Lattice resolved images were obtained from HRTEM and coupled with complementary SAED analysis, enabled reasonable measurements of lattice parameters, characteristic of

defining crystalline planes specific to each of the materials being studied.

Scanning electron microscopy (SEM) and energy dispersive X-ray spectroscopy (EDS). The apparent physical structure, morphology, and average sizes (i.e. diameters) of as-prepared tungstate samples were probed using a field-emission scanning electron microscope (Leo 1550) instrument. The associated EDS analysis was performed to provide elemental composition information, with all of the data collected using an accelerating voltage of 20 kV. Powder samples were dispersed in ethanol and sonicated for about 2 min, prior to their deposition onto an underlying silicon (Si) wafer.

X-ray photoelectron spectroscopy (XPS) measurements. As-prepared tungstate samples were initially dispersed in ethanol, and small aliquots of that solution were deposited onto a Si wafer (measuring 1 cm × 1 cm), followed by evaporative drying in air. Our X-ray photoelectron spectroscopy experiments were carried out within an ultrahigh vacuum (UHV) system, maintaining base pressures of less than $5x\ 10^{-9}$ Torr in a configuration, equipped with a hemispherical electron energy analyzer (SPECS, PHOIBOS 100) and a twin anode X-ray source (SPECS, XR50). To collect the necessary data, a source of Al K_α (1486 eV) was used under irradiation conditions of 13 kV and 30 mA. The angle between the analyzer and the X-ray source was set at 45°. Commercially available CasaXPS software was used to process the collected spectra with the final analyzed results plotted using Origin software.

Synchrotron-based scanning hard X-ray microscopy (SHXM). X-ray microscopy was used to map out variations in chemical composition and structure of our nanorods, integrated over their thickness. Simultaneous x-ray fluorescence (XRF) and differential phase-contrast (DPC) imaging measurements[5-6] were performed using the Nanoscale Multimodal Imaging Instrument (Nano-Mii) located at the Hard X-ray Nanoprobe Beamline[3-4] of the National Synchrotron Light Source

II (NSLS-II), situated at Brookhaven National Laboratory. All pre-fabricated tungstate samples were initially dispersed in ethanol, and tiny aliquots of that solution were deposited onto a specially designed micro sample holder, containing fiducialized grid lines (NCT4155P-III-Cr, Norcada). For the measurements themselves, monochromatic X-rays with an energy of 12 keV were focused to a ~12 nm spot size using Multilayer Laue lenses (MLL).[25-26] Raster imaging was performed using a continuous 'fly-scan' mode, by collecting both transmitted and fluorescence X-ray signals.

The former process resulted in differential phase contrast imaging generated by analyzing the angular shift of the nanobeam interacting with the sample, while the latter data acquisition algorithm enabled insights into elemental maps highlighting the chemical composition of the various samples. PyXRF[27] software was used for producing elemental maps by fitting of the fluorescence spectra.

Synchrotron X-ray fluorescence (XRF) quantification. Quantitative analysis of the elemental composition was conducted on as-obtained SHXM data via MATLAB. The normalized elemental maps produced by PyXRF (accounting for incidence beam normalization) were used as the raw data, i.e. as the 'starting point' for analysis. We used $BaWO_4$ and $SrWO_4$ samples as reference standard samples for scaling Ba, W, and Sr XRF signals. Subsequently, the XRF signals obtained from both the solid-solution and doped nanorod samples were converted into the respective atomic ratios of Ba: W and Sr: W. Data regarding XRF cross-sectional values for Mn were obtained from the XRAYLIB table.

Electrochemical characterization.

Powder samples of as-prepared $BaWO_4$, $BaSrWO_4$, and Mn-$BaWO_4$ were initially dispersed in ethanol with the assistance of sonication to create respective 2 mg/mL inks. The ink

solution was then individually loaded onto a polished glassy carbon electrode (5 mm, Pine Instruments) by dropping two drops (5 μL/drop) of ink onto the electrode. The electrode was subsequently sealed with an ethanolic 0.025% Nafion solution and allowed to dry. Electrochemical measurements were collected in 0.1 M sulfuric acid solutions, created with high-purity type 1 water (with a resistivity value of 18.2 MΩ•cm). A platinum foil served as the counter electrode, and an Ag/AgCl combination was utilized as the reference electrode. Hence, to characterize the electrochemical properties of our as-prepared tungstate samples, cyclic voltammogram (CV) curves were collected within an Ar-saturated electrolyte solution at a scan rate of 20 mV/s for 300 cycles.

3. Results & Discussion

Relevant experimental details about sample preparation and physical characterization techniques used in this study are provided in the Experimental section, as these are well established and have been discussed in prior publications. We focus herein on interpretation of the data sets, collected from these parallel but related efforts.

3.1. Structural and composition characterization of as-prepared tungstate nanorods

XRD was initially performed on all nanorod tungstate samples not only to verify chemical composition but also to determine the generation of the desired crystal structure. Overall, these data corroborate our intended nanorod sample formation. Specifically, Figure 1 shows both survey (2θ range from 10^o to 90^o) and magnified (2θ range from 25^o to 29^o) diffraction patterns, obtained from doped Mn-doped $BaWO_4$ (blue line), $BaWO_4$ control (red line), solid-solution $BaSrWO_4$ (green line), and $SrWO_4$ control (yellow line) samples, respectively. All of the as-obtained patterns for Ba-based samples can be indexed to the body-

centered tetragonal phase (space group $I4_1/a$) of pure $BaWO_4$ (JCPDS No. 080457). Moreover, the $SrWO_4$ control sample also possesses the body-centered tetragonal structure by comparison with the standard pattern (JCPDS No. 080490), with little if any impurities observed (Figure S2).

To highlight the viability of substituting Sr for Ba in creating a chemically stable entity, the region associated with the 2θ values for the (112) peaks of the solid-solution $Ba_xSr_{1-x}WO_4$ sample has been magnified. Specifically, the peaks gradually shift to a higher position according to the sequence of $BaWO_4$ (26.68^o) < $BaSrWO_4$ (27.02^o) < $SrWO_4$ (28.06^o), following the same trend observed for (004). The corresponding, calculated lattice constants of the unit cells slightly decreased in the order of $a(BaWO_4)$ = 5.59 Å > $a(BaSrWO_4)$ = 5.51 Å > $a(SrWO_4)$ = 5.39 Å. The expected increase in the peak position coupled with the anticipated reduction in the lattice cell parameter have been previously reported and collectively confirm the projected unit cell contraction, induced by the partial substitution of Sr for Ba.

Additionally, according to Vegard's Law (Equation 1), the calculated lattice parameter *a* for $Ba_xSr_{1-x}WO_4$ nanorods, assuming a tetragonal structure, was found to vary not only predictably but also monotonically with chemical composition, as follows.[10]

$$a(Ba_xSr_{1-x}WO_4) = a(BaWO_4) + (1 - x)\,[\,a(SrWO_4) - a(BaWO_4)] \qquad \text{(Equation 1)}$$

The calculated results implied a 0.5: 0.5 Ba: Sr ratio for our as-prepared $BaSrWO_4$ sample, consistent with the molar quantities of the Sr and Ba precursors used to make this material.

For the samples doped with Mn, no apparent Mn-containing impurities, such as Mn oxides, were detected. Furthermore, we did not note any peaks which could be convincingly ascribed to $MnWO_4$, thereby confirming the relatively high purity of the sample. Similarly, upon comparing the peak positions of doped Mn-$BaWO_4$ with that of pure $BaWO_4$ alone, we did not observe any perceptible peak shift either for the (112) peak (i.e., $26.72^o \pm 0.02^o$ versus $26.68^o \pm$

0.02 °) or for the (004) peak (i.e., 28.28 ° ± 0.02 ° versus 28.27° ± 0.02 °). The calculated lattice constant *a* value for doped Mn-$BaWO_4$ remained essentially unchanged (*a* = 5.56 Å) as compared with that for pristine $BaWO_4$ (*a* = 5.59 Å). The slight decrease may have been attributable either to a calculation or to an instrumentation error.[11] Nevertheless, it is reasonable to assert that the presence of the additional Mn dopant did not perceptibly alter the underlying AWO_4 scheelite crystal structure.

To generate further insights into the elemental composition of both solid-solution $BaSrWO_4$ and doped Mn-$BaWO_4$ nanorods, SEM-EDS spectra were acquired so as to quantify the overall amounts of each of the individual elements. Because the Sr *L* transition peak (at 1.81 keV) substantially overlaps with the W *M* transition signal (at 1.77 keV) and thereby renders the quantification of $SrWO_4$ as relatively imprecise, we chose to use $BaWO_4$ as the main control sample. As shown in Figure S3, signals associated with the Ba *L*, the W *M*, the W *L*, the Mn *K-alpha*, and the O *K-alpha* transitions were all detected within the as-prepared tungstate samples. The tiny peak for Na impurities likely originates from the Na_2WO_4 reagent.

To compare the concentrations of each metal within the various samples, Table 1 is included. From the SEM-EDS spectra, the atomic content of Ba varied from 17.2% (± 1.7%), 10.5% (± 1.0%), to 15.9% (± 1.6%), in agreement with the theoretical values of 16.7%, 8.3%, and 16.4% for $BaWO_4$, solid-solution $BaSrWO_4$, and doped Mn-$BaWO_4$ samples, respectively. With $BaSrWO_4$, it should be reiterated that because the peak for the Sr *L* transition located at 1.81 keV overlaps with the corresponding W *M* transition, situated at ~1.77 keV, this degree of peak coincidence may contribute to the slight deviation between the experimental and theoretical results with respect to Ba content. Moreover, for the doped Mn-$BaWO_4$ sample, the molar ratio between Mn and Ba was found to be 4.2% ± 0.9%, which is somewhat lower than the expected

ratio (10%), based on the initial starting reagent concentrations. This incomplete incorporation of Mn content was observed previously not only for tungstates[11] but also for other analogous metal oxides, such as Zn_2SiO_4.[28] Overall, we should note that the as-obtained barium: tungsten ratios within each of our as-prepared nanorod samples are very close to the anticipated theoretical amounts. Hence, our SEM-EDS data corroborate our XRD results, and these are consistent with the projected chemical compositions for not only the $BaWO_4$ control sample but also, more significantly, the $BaSrWO_4$ and Mn-$BaWO_4$ test samples.

3.2. Morphological characterization of as-prepared tungstate nanorods

Electron microscopy techniques (such as SEM and TEM) can be used to examine the morphology and size of as-synthesized tungsten nanorods. The series of Figure 2 (A-C) highlights representative SEM images of our as-fabricated tungstate samples. It appears that all of these samples possess anisotropic one-dimensional (1D) structures with not only homogeneous size distributions but also little if any morphological impurities (such as particles) noted. Though some nanorods are broken, this observation can mainly be explained by damage induced by sonication during the washing step. Moreover, no obvious differences existed within each series of samples, suggesting the flexibility, viability, and generalizability of our facile U-tube methods with respect to creating multiple chemically distinctive types of nanorod systems.

TEM (Figure 2D-2F) was used to quantify the dimensions of our as-prepared nanorods. It appears that all of our nanorods maintain an average diameter of ~215 ± 12 nm, consistent with the originating membrane pore channel size of 200 nm. Measured nanorod lengths range from 2.1 to 3.2 μm, which is considerably shorter than the template membrane thickness of 6 μm and which may be attributable either to the limited reaction times used or to fragmentation, resulting from the sonication process. As can be seen from the high-magnification TEM images (Figure

2G-2H), the *d*-spacing values, corresponding to the (112) facet, decreased from 0.331 nm to 0.325 nm in moving from $BaWO_4$ to $BaSrWO_4$ nanorods. As we stated earlier, the lattice spacing diminution can be plausibly explained by the unit cell contraction, emanating from the partial substitution of Sr for Ba within the underlying tungstate lattice. This *d*-spacing decrease matches the corresponding peak position shift noted with the XRD data. The perfectly aligned crystalline planes within individual nanorods of both $BaWO_4$ control and $BaSrWO_4$ solid-solution samples are consistent with their single-crystalline nature. This highly-crystalline character of these nanorods was also corroborated by the discrete and well-defined spots, observed in their corresponding SAED patterns (Figure 2J-2K).[29]

By contrast, Mn-doping of the tungstate lattice yields a different set of characteristic signatures (Figure 2I, 2L). Specifically, the *d*-spacing associated with the (112) facet reduces from 0.331 nm to 0.321 nm, and this observation is coupled with the appearance of an additional (004) facet characterized by a *d*-spacing value of 0.313 nm. More importantly, instead of evincing bright and sharp diffraction dots in the SAED pattern, which would have been characteristic of a single-crystalline material, the Mn-doped sample was actually polycrystalline and it was associated with a more diffuse ring-like SAED pattern.[30] Indeed, the introduction of a non-alkaline-earth-metal, such as Mn, may have interrupted the regular grain orientation and ordered structure of the underlying scheelite crystal lattice, thereby leading to an increased degree of polycrystallinity.

3.3. Electronic structure investigation of surface elements

XPS is considered to be a "surface-sensitive" technique, and can be used to provide information about chemical composition and elemental oxidation states of species at the *surfaces* (~top-most 10 nm) of our as-prepared tungstate nanorods. XPS typically cannot generate usable

chemically relevant data about the composition of either the bulk or the inner core of a sample. In our experiments, survey spectra for each sample were acquired (Figure S4), not only to examine the purity of each sample but also to calibrate the relative peak positions for all of the expected elements associated with the tungstate nanorods. Specifically, the C *1s* peak (derived from air contamination) was set at a fixed position of 284.5 eV,[31] with no other apparent impurities detected.

Figure 3A-3F presents the de-convolution results associated with the Ba *3d* and W *4f* doublet peaks for as-synthesized tungstates. For the $BaWO_4$ control samples, peaks located at 795.7 eV and 780.5 eV could be assigned to Ba *3d*, whereas signals localized at 37.7 eV and 35.7 eV could be ascribed to a W *4f* orbital. In addition, we note that Ba *3d* peaks situated at 795.3 eV and 780.1 eV coupled with the W *4f* peaks found at 37.5 eV and 35.5 eV were measured for the solid-solution $BaSrWO_4$ sample. The relatively small deviation in peak position (i.e., < 0.5 eV) between the control and the mixed stoichiometry samples can be ignored. Moreover, in accordance with the anticipated formation of a solid solution sample, we also detected a doublet peak, positioned at 135.1 eV and 133.3 eV, consistent with the successful incorporation of Sr (Figure 3G).[32] With respect to the doped samples of Mn-$BaWO_4$, peaks located at 795.4 eV and 780.1 eV could be attributed to the Ba *3d* orbital, with corresponding signals at 38.3 eV and 36.2 eV, likely associated with the W *4f* orbital. An additional broadened peak (Figure 3H) centered at ~642.8 eV was consistent with the presence of the Mn dopant.

To summarize, with respect to peak positions, binding energy values for Ba *3d* and W *4f* remained essentially unchanged within all of our as-synthesized tungstates, suggesting that the nominal oxidation states of not only the tungstate cation (i.e., +6) but also the alkaline earth metal cations (i.e., +2) did not dramatically alter across the different sample series. Indeed, our

data support the assumption that Ba ions can be readily substituted by Sr ions within stable configurations.[33] Overall, these data are consistent with conservation of the electronic integrity of the underlying tungstate lattice, which was maintained even after Sr substitution of Ba.

Quantitative data are presented in Table 1 for the various samples analyzed. For example, with the solid-solution $BaSrWO_4$ nanorods, the Ba / W ratio of 0.53 / 1 (± 0.01), as determined from XPS, agrees reasonably well with the corresponding value of 0.59 / 1 (± 0.08), obtained from SEM-EDS. This 'coincidence' strongly suggests a relatively even and homogeneous dispersion of Ba within the solid-solution nanorod, because the chemical compositions of both the outer shell and the inner bulk appear to be reasonably close in magnitude. In addition, the computed Ba / Sr ratio, generated from XPS, was found to be 1 / 1.15 (± 0.02) within the mixed stoichiometry nanorod sample, a value consistent with the substitution of Ba cations with Sr. It is worth emphasizing the significance of XPS in assessing Sr content, since with SEM-EDS, the Sr and W signals overlap to some degree and hence, it is more difficult to achieve a conclusive result with that technique.

With respect to the doped Mn-$BaWO_4$, the Ba / W value (i.e., 1.21 / 1(± 0.02)) derived from XPS is relatively consistent with but is definitely larger as compared not only with data (i.e., 0.95 / 1 (± 0.01)) obtained from SEM-EDS but also with theoretical expectations (1/1). We cannot fully explain this larger Ba: W ratio, based on interpreting XPS data alone. Interestingly, when analyzing the Mn content in these samples, the surface Mn concentration, calculated from XPS was found to be ~ 2 times larger than that noted from the interior bulk, as found from SEM-EDS. This result implies either surface segregation or aggregation of the Mn dopant ions occurring, a situation which may have originated from the actual formation process of the

tungstate nanorods themselves. Significantly, we should note that XPS data alone cannot readily distinguish between a 'uniform' versus an 'uneven' surface segregation and aggregation.

3.4. Morphology and chemical composition of as-prepared tungstate nanorods, as derived form SHXM-XRF

Thus far, we have seen herein that whereas XRD, SAED, SEM, and HRTEM provide mainly structural (i.e., morphology, lattice parameters, and crystallinity) information about our tungstate nanorods, SEM-EDS and XPS yield complementary data on chemical composition and surface element electronic structure, respectively. As an alternative characterization technique, SHXM offers the possibility of probing the chemical mapping of elements through the full volume of the sample, by contrast with either surface-sensitive XPS or SEM-EDS.[34]

Relevant complementary sets of SHXM data, providing both qualitative and quantitative trends, are shown below. In Figure 4, differential phase contrast (DPC) images with scale bars inserted for each of the samples analyzed are presented in the left-hand-most column. The region within the DPC image correlates with and corresponds to the accompanying fluorescence mapping images of the identical specimen in question, presented for each individual material studied. DPC images represent electron density variations through the entire thickness. We should note that from the DPC images of solid-solution $BaSrWO_4$ (panels B1-B5) and of doped Mn-$BaWO_4$ (panels C1-C5) samples, the data indicate the presence of aggregate bundles as opposed to individual nanorods, a finding consistent with our SEM and TEM results. Pure $BaWO_4$ (panels A1-A5) was used as a reference standard for our studies.

In order to elucidate the elemental distribution within both (i) the solid-solution $BaSrWO_4$ and (ii) the doped Mn-$BaWO_4$ samples, analogous X-ray fluorescence (XRF) mapping images were also collected as part of Figure 4. Specifically, individual signals emanating from

the (a) Ba *L*-edge (red) and (b) W *L*-edge (green) are shown as (a) Figure 4, panels A2, B2, and C2 and (b) Figure 4, panels A3, B3, and C3, respectively. The presence of data from either the Sr *L*-edge or the Mn *K*-edge (derived from the corresponding $BaSrWO_4$ or Mn-$BaWO_4$, respectively) are also included in Figure 4, panels B4, and C4, and these are shown as a blue/purple hue.

The merged, consolidated images from all of the extant metals, present in and expected from the tungstate sample, including Ba, Sr, W, and Mn (as applicable) are presented as Figure 4, panels A5, B5, and C5. What is apparent is that the elemental dispersion profiles of the Ba *L*-edge and the W *L*-edge almost perfectly overlap with each other (Figure S5). These results imply that Ba and W atoms are likely to be homogeneously distributed throughout the nanorods, *regardless* of either Sr substitution or Mn doping. With respect to the signals for the Sr *L*-edge and the Mn *K*-edge, our images also suggest a relatively even and uniform distribution of Sr cations and Mn dopant ions within the as-synthesized solid-solution $BaSrWO_4$ and doped Mn-$BaWO_4$ samples, respectively.

Figure 5 and Figure 6 highlight the corresponding quantified data for $BaSrWO_4$, and Mn-$BaWO_4$, respectively. Detailed processing algorithms were used to generate these data. In effect, $BaWO_4$ and $SrWO_4$ were utilized as the reference standards (Figure S6). Relevant parameters related to the Welch's t-test for each sample are summarized in Table S1. We describe our efforts in more detail in the Supporting Information. These quantification results are summarized and compared with corresponding data derived from other characterization techniques in Table 1. It is noteworthy that since the absorption for X-rays in the nanorods is negligible, the cumulative X-ray data provide for better representative values of the atomic ratio throughout the entire thickness, even when multiple nanorods are stacked together.

Based upon our SHXM-XRF data interpretation, the following observations were noted. (1) For the solid-solution $BaSrWO_4$ sample, Ba and W signals essentially perfectly overlap with and are coincident with each other. The corresponding Ba: W ratio was calculated to be 0.50, which is slightly lower than but certainly within the same range as the values derived from either SEM-EDS (i.e., 0.59) or XPS (i.e., 0.53). Nevertheless, what is noteworthy is that the Ba: W ratio obtained from synchrotron XRF measurements perfectly corresponded, within error, with the theoretically expected value of 0.50, derived from the chemical formula. With respect to the computed Ba / Sr ratio, the amount of Sr was slightly higher, as confirmed by both XRF (i.e., 1 / 1.33 (± 0.04)) and XPS (i.e., 1 / 1.15 (± 0.02)) results. As we mentioned previously, the Sr signal overlaps with the W signal within SEM-EDS, and hence is intrinsically more difficult to precisely quantify with that technique. Hence, these overall data substantiate the advantage of utilizing X-ray beam excitation as opposed to merely electron beam excitation to address sources of potential ambiguity, especially in the context of more precisely quantifying the composition of more chemically 'complex' samples such as $BaSrWO_4$ versus simpler controls.

(2) For the doped Mn-$BaWO_4$, the calculated Ba: W ratio is 0.92, and we note that the corresponding figure obtained from SEM-EDS analysis (i.e. 0.95) is similar to that derived result. In addition, the overall concentration of Mn dopant was found to be ~ 5.8% (i.e., molar ratio normalized to Ba), which is close to what was observed by SEM-EDS (i.e., ~ 4.2%), again highlighting a degree of consistency across measurement techniques. Moreover, a relatively homogeneous distribution of Mn within our XRF image (Figure 6B) was detected, thereby confirming the presence of a more 'uniform' as opposed to an uneven spatial distribution of our Mn dopant ions. What we should emphasize is that the amount of Mn detected by XPS was clearly higher than that found using other techniques. This elemental variation can be potentially

ascribed to the preferential spatial localization and aggregation of Mn ions on the nanorod surface, since XPS is particularly surface sensitive. Nonetheless, to be clear, for the Mn-$BaWO_4$ sample, the overall elemental amounts, derived from both SEM-EDS and SHXM-XRF analyses, concur with each other. The XRF mapping profiles were indicative of the relatively uniform spatial distribution of each element.

3.5. Electrochemical performance of Ba-based tungstates as support material

As we have previously alluded to, metal oxides have been widely explored as catalyst supports for the methanol oxidation reaction, and hence, the intrinsic stability of the support material may dramatically affect the overall catalytic performance.[35] Therefore, as a demonstration of principle of this idea, the electrochemical durability of our as-prepared tungstate nanorods within acidic electrolyte was also evaluated, prior to the actual MOR measurement. Specifically, the stability of $BaSrWO_4$ and Mn-$BaWO_4$ samples was assessed by cycling each sample within an argon-saturated 0.1 M sulfuric acid solution for 300 cycles at a scan rate of 20 mV/s. The collected CVs (Figure S7) indicated that both samples possessed reasonable durability, since the shape of the CV curve after cycle 300 was very similar to that of cycle 1. A slight increase in current was observed for both samples as well as for the $BaWO_4$ control, an observation which could be potentially ascribed to the surface roughening of the nanorod during the cycling procedure itself. Though no obvious oxygen adsorption features were detected for the Ba-based tungstates, the apparently high durability of all of our nanorod samples within acidic media may provide for stable binding sites for metal catalysts during electrochemical processing,[12] thereby rendering the possibility for their use as viable catalyst supports for electro-oxidation reactions.

How does the observed electrochemical stability correlate with the chemical composition of the tungstates, as deduced from our characterization data? It turns out that for both $BaSrWO_4$ and Mn-$BaWO_4$ nanorods, our collective microscopy and spectroscopy results confirmed that (a) the inherent underlying crystal structure was preserved, and that (b) there is a homogeneous elemental spatial distribution within these samples, regardless of either cationic substitution or cationic doping. These observations strongly suggest that the intrinsic durability of scheelite-based tungstate nanorods is independent of subtle changes in chemical composition alone. As the basis of future work and efforts in our lab, we plan to more thoroughly investigate the same question of how subtle changes in chemical composition and elemental distribution within metal oxides can affect and impact favorable, synergistic catalyst (such as Pt) - support interactions.[36]

4. Conclusions

Our work with SHXM has demonstrated its ability to map out elemental distributions within anisotropic nanorod configurations with the possibility of precise quantification. Hence, what specific advantages does SHXM possess?

(1) Lesser sample quantities needed coupled with a relatively rapid and facile sample preparation process. Whereas the combination of SEM-EDS can be used to probe both morphology and elemental quantification, sample thicknesses necessary for this process need to be sizeable in order to obtain a reasonable signal. By contrast, SHXM has shown the capability of analyzing either small numbers/aggregates of or even individual nanorods.

(2) More accurate sample representation. Because of the relatively deep penetrating capabilities of X-rays (with respect to electron beam for instance), acquired DPC images from SHXM reflect holistic measurements of the ‘entire’ sample volume with the corresponding potential for

collecting stronger XRF 'signal-to-noise' data sets. By contrast, electron microscopy data tend to provide complementary information mainly focused on surface properties.

(3) Greater elemental sensitivity with high spatial resolution. Using a compilation of qualitative fluorescence mapping images coupled with normalized, quantifiable intensity data, we were able not only to observe the elemental distribution through the entire sample but also to gain insights into elemental concentration, even for samples with relatively low dopant levels. As a concrete example, the precise chemical composition of the solid-solution $BaSrWO_4$ sample cannot be adequately evaluated using SEM-EDS alone, due to signal overlapping problems. Hence, our experiments highlight the beneficial capability of SHXM with respect to the crucial issue of elemental quantification, as uniquely applied to one-dimensional nanorods.

Overall, our data prove the promise and potential of SHXM in providing both relevant structural and chemical composition information about nanoscale systems. In particular, we have found that our SHXM data are fully consistent with, complement, and aid in the interpretation of conventional SEM, TEM, XRD, SAED, and XPS results. Specifically, herein we have used SHXM to map out, analyze, and interpret the elemental distribution within alkaline-earth-metal tungstate nanorods with a combination of qualitative and quantitative imaging results. In addition, the stability of the nanorods in acidic electrolyte was confirmed by CV curves and confirm the possibility of using these nanorods as catalyst support materials with respect to electro-oxidation reactions in fuel cell. Indeed, our data strongly imply that the intrinsic durability of scheelite-based tungstate nanorods is likely to be independent of subtle changes in chemical composition alone. In terms of future work, beyond the scope of the current study, we envision that the localized chemical and physical information obtainable by SHXM can enable the development of

strategies for fully understanding, predicting, and optimizing structure-property correlations, relevant for applications such as electrocatalysis.

Supporting Information Available

Additional information on SHXM-XRF data interpretation protocols; schematic of the experimental setup used; XRD patterns; SEM-EDS data, in addition to complementary XPS and SHXM characterization data (including a Table) acquired for the samples analyzed, including reference control samples; along with preliminary cyclic voltammetry data. This material is available free of charge via the Internet at http://pubs.acs.org.

Acknowledgements

This material is based on work supported by the U.S. National Science Foundation under Grant No. CHE-1807640. Structural characterization experiments (TEM, SEM, and XPS) for this manuscript were performed in part at the Center for Functional Nanomaterials, located at Brookhaven National Laboratory, which is supported by the U.S. Department of Energy under Contract No. DE-SC-00112704. This research also used the Hard X-ray Nanoprobe Beamline at 3-ID of the National Synchrotron Light Source II, a U.S. Department of Energy (DOE) Office of Science User Facility operated for the DOE Office of Science by Brookhaven National Laboratory under Contract No. DE-SC0012704.

References

1. Wang, L.;Zhou, Y.;Timoshenko, J.;Liu, S.;Qiao, Q.;Kisslinger, K.;Cuiffo, M.;Chuang, Y. C.;Zuo, X.;Xue, Y., et al. Designing Nanoplatelet Alloy/Nafion Catalytic Interface for Optimization of PEMFCs: Performance, Durability, and CO Resistance. *ACS Catal.* **2019,** *9*, 1446-1456.
2. Li, L.;Wong, S. S. Ultrathin Metallic Nanowire-Based Architectures as High-Performing Electrocatalysts. *ACS Omega* **2018,** *3*, 3294−3313
3. Yan, H.;Bouet, N.;Zhou, J.;Huang, X.;Nazaretski, E.;Xu, W.;Cocco, A. P.;Chiu, W.;Brinkman, K. S.;Chu, Y. S. Multimodal Hard X-ray Imaging with Resolution Approaching 10 nm for Studies in Material Science. *Nano Futures* **2018,** *2*, 011001(1-9).
4. Nazaretski, E.;Yan, H.;Lauer, K.;Bouet, N.;Huang, X.;Xu, W.;Zhou, J.;Shu, D.;Hwu, Y.;Chu, Y. S. Design and Performance of an X-ray Scanning Microscope at the Hard X-ray Nanoprobe Beamline of NSLS-II. *J. Synchrotron Radiat.* **2017,** *24*, 1113-1119.
5. Yan, H.;Chu, Y. S.;Maser, J.;Nazaretski, E.;Kim, J.;Kang, H. C.;Lombardo, J. J.;Chiu, W. K. Quantitative X-ray Phase Imaging at the Nanoscale by Multilayer Laue Lenses. *Sci. Rep.* **2013,** *3*, 1307(1-5)
6. Yan, H.;Nazaretski, E.;Lauer, K.;Huang, X.;Wagner, U.;Rau, C.;Yusuf, M.;Robinson, I.;Kalbfleisch, S.;Li, L., et al. Multimodality Hard-X-ray Imaging of a Chromosome with Nanoscale Spatial Resolution. *Sci. Rep.* **2016,** *6*, 20112(1-7).
7. Saito, N.;Sonoyama, N.;Sakata, T. Analysis of the Excitation and Emission Spectra of Tungstates and Molybdate. *Bull. Chem. Soc. Jpn.* **1996,** *69*, 2191 - 2194.
8. Liao, H.;Wang, Y.;Liu, X.;Li, Y.;Qian, Y. Hydrothermal Preparation and Characterization of Luminescent $CdWO_4$ Nanorods. *Chem. Mater.* **2000,** *12*, 2819-2821.
9. Kloprogge, J. T.;Weier, M. L.;Duong, L. V.;Frost, R. L. Microwave-Assisted Synthesis and Characterisation of Divalent Metal Tungstate Nanocrystalline Minerals: Ferberite, Hübnerite, Sanmartinite, Scheelite and Stolzite. *Mater. Chem. Phys.* **2004,** *88*, 438-443.
10. Zhang, F.;Sfeir, M. Y.;Misewich, J. A.;Wong, S. S. Room-Temperature Preparation, Characterization, and Photoluminescence Measurements of Solid Solutions of Various Compositionally-Defined Single-Crystalline Alkaline-Earth-Metal Tungstate Nanorods. *Chem. Mater.* **2008,** *20*, 5500–5512.
11. Zhang, F.;Yiu, Y.;Aronson, M. C.;Wong, S. S. Exploring the Room-Temperature Synthesis and Properties of Multifunctional Doped Tungstate Nanorods. *J. Phys. Chem. C* **2008,** *112*, 14816-14824.
12. Scofield, M. E.;Koenigsmann, C.;Bobb-Semple, D.;Tao, J.;Tong, X.;Wang, L.;Lewis, C. S.;Vukmirovic, M. B.;Zhu, Y.;Adzicd, R. R., et al. Correlating the Chemical Composition and Size of Various Metal Oxide Substrates with the Catalytic Activity and Stability of As-Deposited Pt Nanoparticles for the Methanol Oxidation Reaction. *Catal. Sci. Technol.* **2016,** *6*, 2435–2450.
13. Scofield, M. E.;Liu, H.;Wong, S. S. A Concise Guide to Sustainable PEMFCs: Recent Advances in Improving Both Oxygen Reduction Catalysts and Proton Exchange Membranes. *Chem. Soc. Rev.* **2015,** *44*, 5836-5860.
14. Sharma, S.;Pollet, B. G. Support Materials for PEMFC and DMFC Electrocatalysts—A Review. *J. Power Sources* **2012,** *208*, 96-119.
15. Maiyalagan, T.;Viswanathan, B. Catalytic Activity of Platinum/Tungsten Oxide Nanorod Electrodes towards Electro-Oxidation of Methanol. *J. Power Sources* **2008,** *175*, 789–793.

16. Li, F.;Gong, H.;Wang, Y.;Zhang, H.;Wang, Y.;Liu, S.;Wang, S.;Sun, C. Enhanced Activity, Durability and Anti-Poisoning Property of Pt/$W_{18}O_{49}$ for Methanol Oxidation with a Sub-Stoichiometric Tungsten Oxide $W_{18}O_{49}$ Support. *J. Mater. Chem. A* **2014,** *2*, 20154-20163.
17. Jayaraman, S.;Jaramillo, T. F.;Baeck, S.-H.;McFarland, E. W. Synthesis and Characterization of Pt-WO_3 as Methanol Oxidation Catalysts for Fuel Cells. *J. Phys. Chem. B* **2005,** *109*, 22958-22966.
18. Liu, X.;Nie, Y.;Yang, H.;Sun, S.;Chen, Y.;Yang, T.;Lin, S. Enhancement of the Photocatalytic Activity and Electrochemical Property of Graphene-$SrWO_4$ Nanocomposite. *Solid State Sci.* **2016,** *55*, 130-137.
19. Araba, M.;Lopes-Moriyama, A.;Santos, T.;Souzab, C.;Gavarria, J.;Leroux, C. Strontium and Cerium Tungstate Materials $SrWO_4$ and $Ce_2(WO_4)_3$: Methane Oxidation and Mixed Conduction. *Catal. Today* **2013,** *208*, 35– 41.
20. Passos, R.;Souza, C.;Leroux, C.;Arab, M. Catalytic Properties of $Sr_{1-x}Ce_xWO_4$: The Role of Mixed Conduction in Methane Oxidation. *Int. J. Hydrogen Energy* **2018,** *43*, 15918-15930.
21. Yu, C.;Guo, X.;Xi, Z.;Muzzio, M.;Yin, Z.;Shen, B.;Li, J.;Seto, C. T.;Sun, S. AgPd Nanoparticles Deposited on $WO_{2.72}$ Nanorods as an Efficient Catalyst for One-Pot Conversion of Nitrophenol/Nitroacetophenone into Benzoxazole/Quinazoline. *J. Am. Chem. Soc.* **2017,** *139*, 5712-5715.
22. Tiwari, A.;Singh, V.;Nagaiah, T. C. Tuning the $MnWO_4$ Morphology and Its Electrocatalytic Activity towards Oxygen Reduction Reaction. *J. Mater. Chem. A* **2018,** *6*, 2681-2692.
23. Farsi, H.;Barzgari, Z. Synthesis, Characterization, and Electrochemical Studies of Nanostructured $CaWO_4$ as Platinum Support for Oxygen Reduction Reaction. *Mater. Res. Bull.* **2014,** *59*, 261-268.
24. Yue, S.;Zhou, Y.;Zou, S.;Wang, L.;Liu, H.;Wong, S. S. Chemically Tunable, All-Inorganic-Based White-Light Emitting 0D–1D Heterostructures. *Adv. Optical Mater.* **2017,** *5*, 1700089 (1-18).
25. Huang, X.;Yan, H.;Nazaretski, E.;Conley, R.;Bouet, N.;Zhou, J.;Lauer, K.;Li, L.;Eom, D.;Legnini, D., et al. 11 nm Hard X-ray Focus from a Large-Aperture Multilayer Laue Lens. *Sci. Rep.* **2013,** *3*, 3562(1-5).
26. Yan, H.;Conley, R.;Bouet, N.;Chu, Y. S. Hard X-ray Nanofocusing by Multilayer Laue Lenses. *J. Phys. D: Appl. Phys.* **2014,** *47*, 263001(1-31).
27. Li, L.;Yan, H.;Xu, W.;Yu, D.;Heroux, A.;Lee, W.;Campbell, S. I.;Chu, Y. S. PyxRF: Python-Based X-ray Fluorescence Analysis Package. *Proc. SPIE 10389, X-ray Nanoimaging: Instruments and Methods III* **2017**, 103890.
28. Liu, H.;Moronta, D.;Li, L.;Yue, S.;Wong, S. S. Synthesis, Properties, and Formation Mechanism of Mn-Doped Zn_2SiO_4 Nanowires and Associated Heterostructures. *Phys. Chem. Chem. Phys.* **2018,** *20*, 10086-10099.
29. Sasidharan, S.;Shyni, P., C. ;Chaudhary, N.;Ramakrishnan, V. Single Crystal Organic Nanoflowers. *Sci. Rep.* **2017,** *7*, 17335(1-8).
30. Liu, H.;Adzic, R. R.;Wong, S. S. Multifunctional Ultrathin Pd_xCu_{1-x} and $Pt_{\backsim}Pd_xCu_{1-x}$ One-Dimensional Nanowire Motifs for Various Small Molecule Oxidation Reactions. *ACS Appl. Mater. Interfaces* **2015,** *7*, 26145-26157.
31. Li, L.;Liu, H.;Qin, C.;Liang, Z.;Scida, A.;Yue, S.;Tong, X.;Adzic, R. R.;Wong, S. S. Ultrathin Pt_xSn_{1-x} Nanowires for Methanol and Ethanol Oxidation Reactions: Tuning Performance by Varying Chemical Composition. *ACS Appl. Nano Mater.* **2018,** *1*, 1104-1115.

32. Huang, J.;Li, Q.;Wang, J.;Jin, L.;Tian, B.;Li, C.;Shi, Y.;Wang, Z.;Hao, J. Controllable Synthesis of Lanthanide Yb^{3+} and Er^{3+} Co-doped AWO_4 (A = Ca, Sr, Ba) Micro-Structured Materials: Phase, Morphology and Up-Conversion Luminescence Enhancement. *Dalton Trans.* **2018,** *47*, 8611-8618.
33. Culver, S. P.;Greaney, M. J.;Tinoco, A.;Brutchey, R. L. Low-Temperature Synthesis of Homogeneous Solid Solutions of Scheelite-Structured $Ca_{1-x}Sr_xWO_4$ and $Ba_{1-x}Sr_xWO_4$ nanocrystals. *Dalton Trans.* **2015,** *44*, 15042-15048.
34. Kang, H. C.;Yan, H.;Chu, Y. S.;Lee, S. Y.;Kim, J.;Nazaretski, E.;Kim, C.;Seo, O.;Noh do, Y.;Macrander, A. T., et al. Oxidation of PtNi Nanoparticles Studied by A Scanning X-ray Fluorescence Microscope with Multi-layer Laue Lenses. *Nanoscale* **2013,** *5*, 7184-7187.
35. Li, L.;Tan, S.;Salvatore, K. L.;Wong, S. S. Nanoscale Perovskites as Catalysts and Supports for Direct Methanol Fuel Cells. *Chemistry* **2019,** *in press DOI: 10.1002/chem.201805695*.
36. Tao, L.;Shi, Y.;Huang, Y.-C.;Chen, R.;Zhang, Y.;Huo, J.;Zou, Y.;Yu, G.;Luo, J.;Dong, C.-L., et al. Interface Engineering of Pt and CeO_2 Nanorods with Unique Interaction for Methanol Oxidation. *Nano Energy* **2018,** *53*, 604-612.

Figure Captions

Figure 1. (A) Survey XRD spectra coupled with (B) magnified views of the (112) peak associated with as-prepared samples of doped Mn-$BaWO_4$ (blue), $BaWO_4$ (red), solid-solution $BaSrWO_4$ (green), and $SrWO_4$ (yellow). Facets have been indexed, according to the JCPDS No. 080457 database standard for $BaWO_4$.

Figure 2. (A, B, C) SEM images; (D, E, F) low-resolution TEM images; (G, H, I) high-resolution TEM images; and (J, K, L) the corresponding SAED patterns (with TEM images of the sample areas analyzed as insets) of (A, D, G, J) $BaWO_4$, (B, E, H, K) solid-solution $BaSrWO_4$, and (C, F, I, L) doped Mn-$BaWO_4$ nanorods, respectively.

Figure 3. XPS spectra of (A, B, C) Ba *3d*; (D, E, F) W *4f*; (G) Sr *3d*; and (H) Mn *2p* orbitals for (A, D) $BaWO_4$, (B, E, G) solid-solution $BaSrWO_4$, and (C, F, H) doped Mn-$BaWO_4$ nanorods, respectively

Figure 4. SHXM results: Differential phase contrast (DPC) images (panels A1, B1, C1), Ba *L*-edge XRF image (panels A2, B2, C2), W *L*-edge XRF image (panels A3, B3, C3), in addition to Sr *L*-edge (panel B4) and Mn *K*-edge XRF images (panel C4). The merged overlay signals (panels A5, B5, C5) are associated with the sample series, comprised of nanorods of (row A) $BaWO_4$, (row B) solid-solution $BaSrWO_4$, and (row C) doped Mn-$BaWO_4$, respectively. Data were obtained using the Nanoscale Multimodal Imaging (Nano-Mii) Instrument. Scale bars for each of the samples analyzed are represented within the individual DPC images.

Figure 5. SHXM results: (A) Ba intensity, (B) Sr intensity, (C) W intensity, as well as the ratio between (D) Ba/W and (E) Sr/W, associated with $BaSrWO_4$ nanorods.

Figure 6. SHXM results: (A) Ba intensity, (B) Mn intensity, (C) W intensity, as well as the ratio between (D) Ba/W and (E) Mn/W, associated with Mn-$BaWO_4$ nanorods.

Table 1. Summary of quantification results, associated with not only (i) barium, (ii) barium - tungsten atomic ratios but also (iii) barium – strontium/manganese atomic ratios, as derived from SEM-EDS, XPS, and SHXM-XRF experiments, respectively.

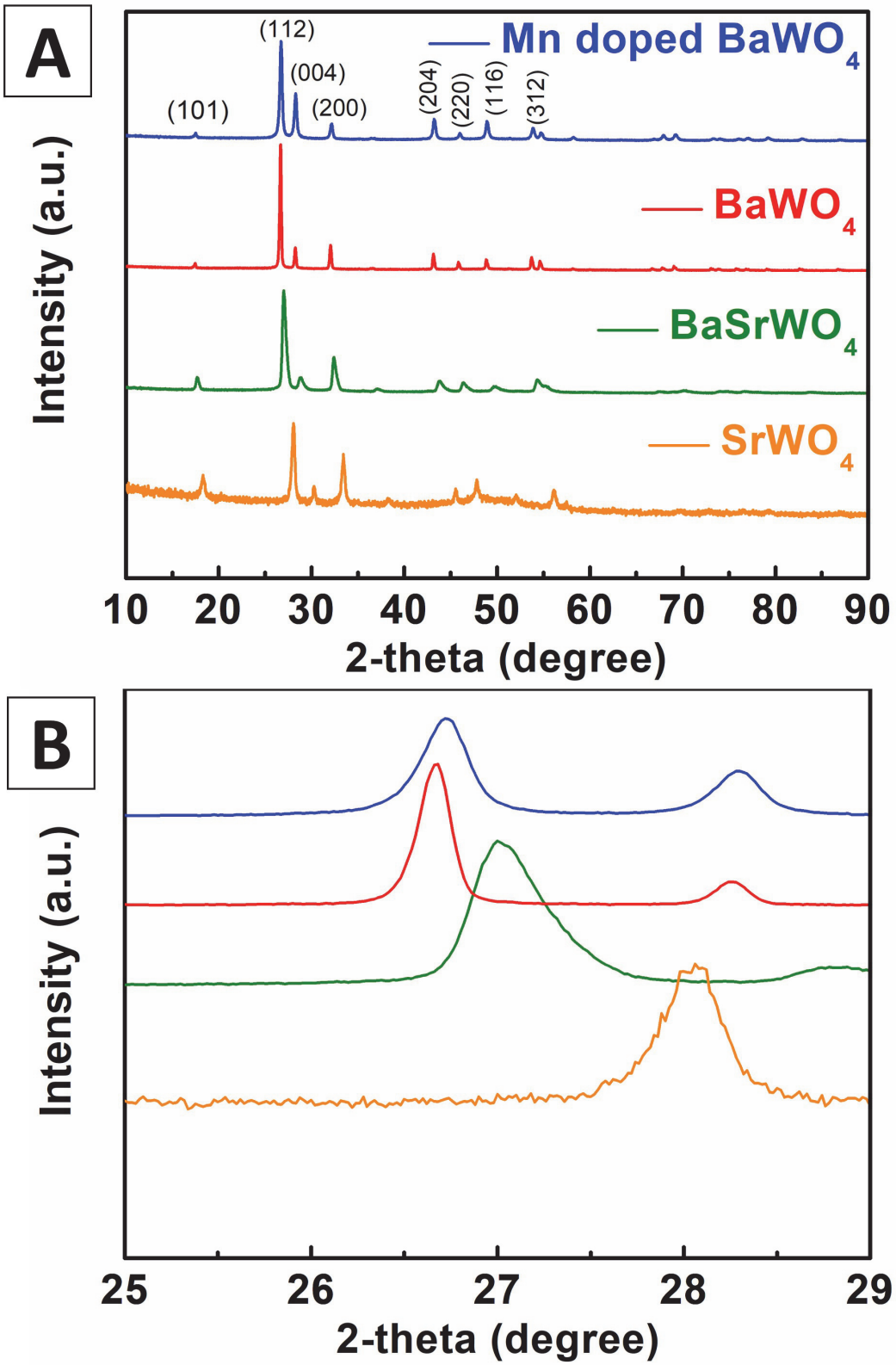
A
(112)
(004)
(200)
(101)
(204)
(220)
(116)
(312)
Mn doped BaWO4
BaWO4
BaSrWO4
SrWO4
Intensity (a.u.)
10 20 30 40 50 60 70 80 90
2-theta (degree)
B
Intensity (a.u.)
25 26 27 28 29
2-theta (degree)

Figure 1.

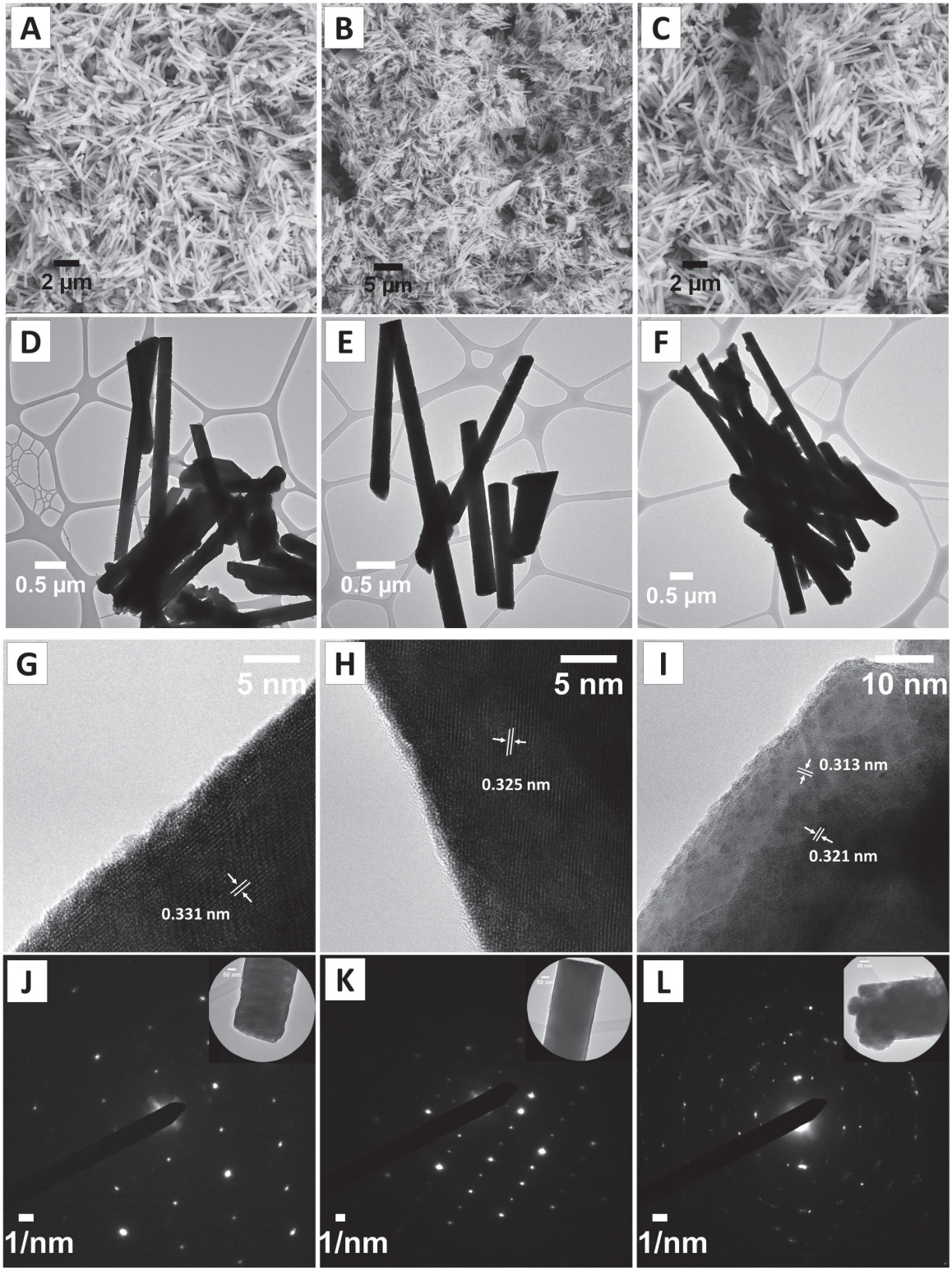
A
2 μm
B
5 μm
C
2 μm
D
0.5 μm
E
0.5 μm
F
0.5 μm
G
5 nm
0.331 nm
H
5 nm
0.325 nm
I
10 nm
0.313 nm
0.321 nm
J
1/nm
K
1/nm
L
1/nm

Figure 2.

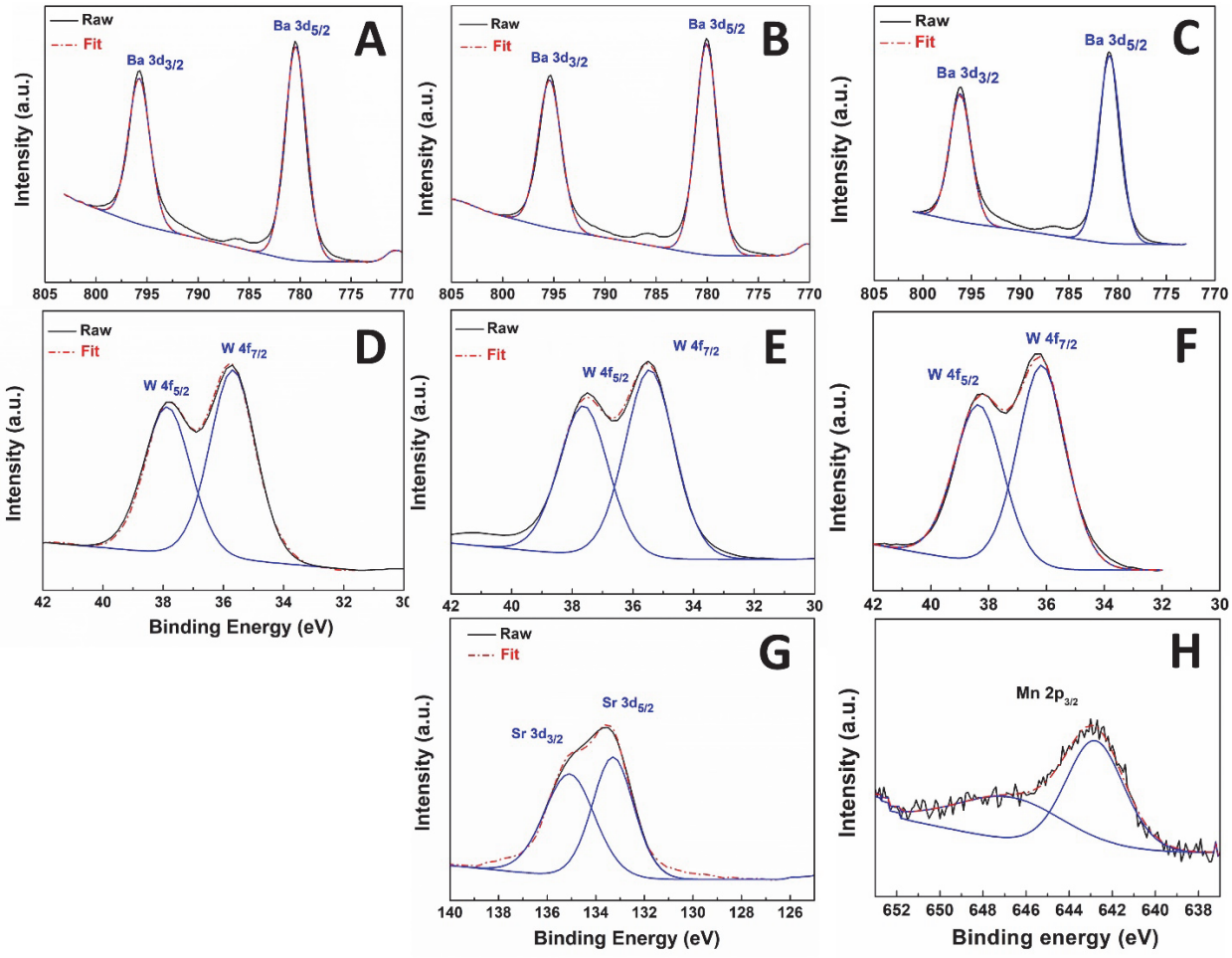
A
Raw
Fit
Ba 3d5/2
Ba 3d3/2
Intensity (a.u.)
805 800 795 790 785 780 775 770
B
Raw
Fit
Ba 3d5/2
Ba 3d3/2
Intensity (a.u.)
805 800 795 790 785 780 775 770
C
Raw
Fit
Ba 3d5/2
Ba 3d3/2
Intensity (a.u.)
805 800 795 790 785 780 775 770
D
Raw
Fit
W 4f7/2
W 4f5/2
Intensity (a.u.)
42 40 38 36 34 32 30
Binding Energy (eV)
E
Raw
Fit
W 4f7/2
W 4f5/2
Intensity (a.u.)
42 40 38 36 34 32 30
F
W 4f7/2
W 4f5/2
Intensity (a.u.)
42 40 38 36 34 32 30
G
Raw
Fit
Sr 3d5/2
Sr 3d3/2
Intensity (a.u.)
140 138 136 134 132 130 128 126
Binding Energy (eV)
H
Mn 2p3/2
Intensity (a.u.)
652 650 648 646 644 642 640 638
Binding energy (eV)

Figure 3.

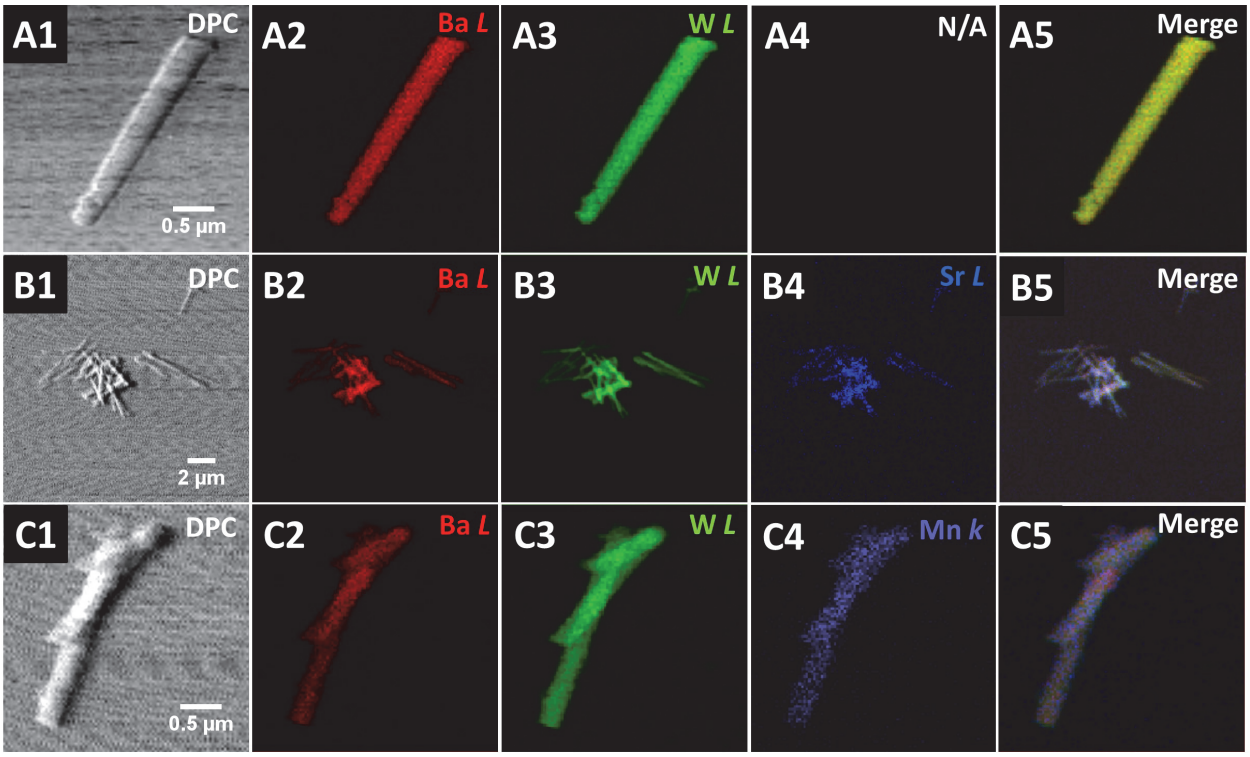
A1
DPC
0.5 µm
A2
Ba L
A3
W L
A4
N/A
A5
Merge
B1
DPC
2 µm
B2
Ba L
B3
W L
B4
Sr L
B5
Merge
C1
DPC
0.5 µm
C2
Ba L
C3
W L
C4
Mn k
C5
Merge

Figure 4.

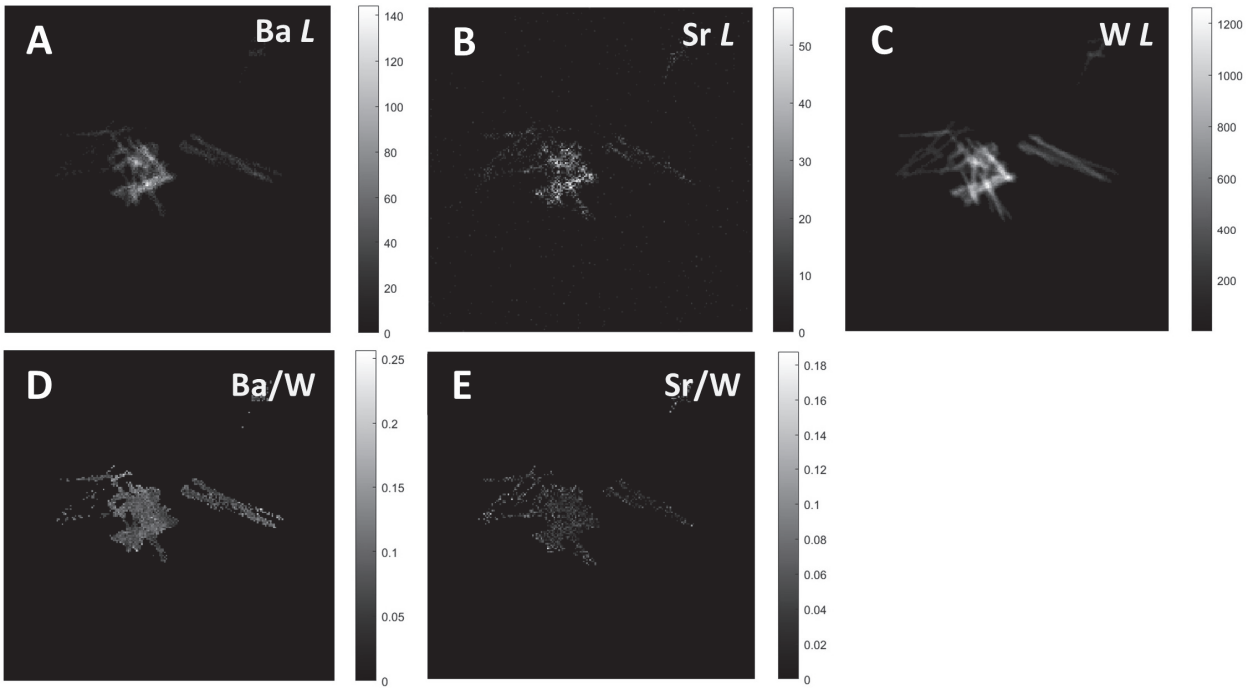
A
Ba L
140
120
100
80
60
40
20
0
B
Sr L
50
40
30
20
10
0
C
W L
1200
1000
800
600
400
200
D
Ba/W
0.25
0.2
0.15
0.1
0.05
0
E
Sr/W
0.18
0.16
0.14
0.12
0.1
0.08
0.06
0.04
0.02
0

Figure 5.

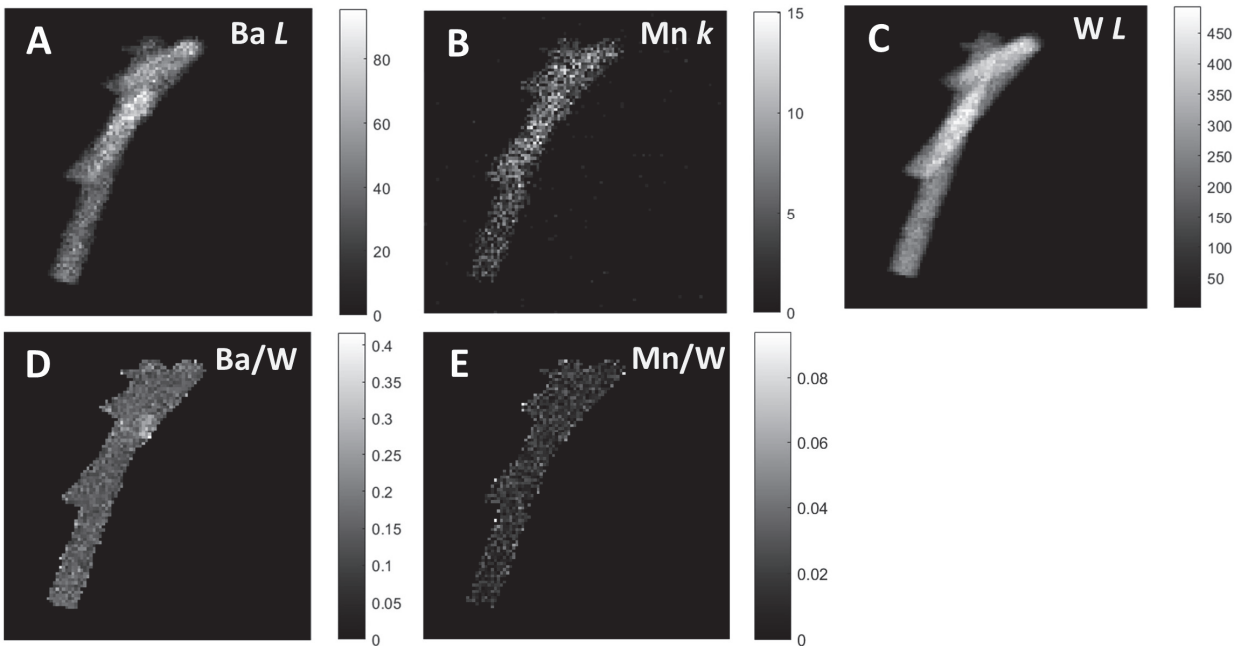
A
Ba L
80
60
40
20
0
B
Mn k
15
10
5
0
C
W L
450
400
350
300
250
200
150
100
50
D
Ba/W
0.4
0.35
0.3
0.25
0.2
0.15
0.1
0.05
0
E
Mn/W
0.08
0.06
0.04
0.02
0

Figure 6.

	SEM-EDS results		XPS results		SHXM-XRF results	
	Ba / W atomic ratio	Ba / M atomic ratio (M = Sr, Mn)	Ba / W atomic ratio	Ba / M atomic ratio (M = Sr, Mn)	Ba / W atomic ratio	Ba / M atomic ratio (M = Sr, Mn)
$BaWO_4$	1.04/ 1 ± 0.05	_	1.07 / 1 ± 0.01	_	1.00 / 1 ± 0.04	_
$Ba_{0.5}Sr_{0.5}WO_4$	0.59 / 1 ± 0.08	_	0.53 / 1 ± 0.01	1 / 1.15 ± 0.02	0.50 / 1 ± 0.02	1 / 1.33 ± 0.04
Mn-doped $BaWO_4$	0.95 / 1 ± 0.01	1 / 0.04 ± 0.01	1.21 / 1 ± 0.02	1 / 0.09 ± 0.12	0.92 / 1 ± 0.04	1 / 0.058

Table 1.

TOC Graphic